Received: 26 October 2020 | Accepted: 14 November 2020

DOI: 10.1002/jnr.24767

RESEARCH ARTICLE

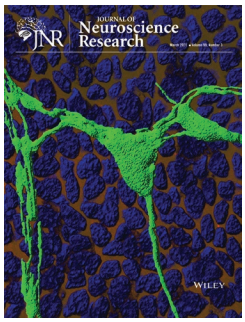

Axonal mitochondria adjust in size depending on *g*-ratio of surrounding myelin during homeostasis and advanced remyelination

Benjamin V. Ineichen[1] | **Keying Zhu**[1] | **Karl E. Carlström**[1,2]

[1]Department of Clinical Neurosciences, Karolinska Institutet, Center for Molecular Medicine, Karolinska Hospital at Solna, Stockholm, Sweden

[2]Laboratory of Molecular Neurobiology, Department Medical Biochemistry and Biophysics, Biomedicum, Karolinska Institutet, Stockholm, Sweden

Correspondence
Karl E. Carlström, Laboratory of molecular Neurobiology, Department of Medical Biochemistry and Biophysics, Biomedicum, Karolinska Institutet C06, Stockholm 9, 171 65 Sweden
Email: karl.carlstrom@ki.se

Funding information
Erik och Edith Fernströms S; Swiss National Science Foundation

Abstract

Demyelinating pathology is common in many neurological diseases such as multiple sclerosis, stroke, and Alzheimer's disease and results in axonal energy deficiency, dysfunctional axonal propagation, and neurodegeneration. During myelin repair and also during myelin homeostasis, mutual regulative processes between axons and myelin sheaths are known to be essential. However, proficient tools are lacking to characterize axon-myelin interdependence during (re)myelination. Thus, we herein investigated adaptions in myelin sheath *g*-ratio as a proxy for myelin thickness and axon metabolic status during homeostasis and myelin repair, by using axonal mitochondrial size as a proxy for axonal metabolic status. We found that axons with thinner myelin sheaths had larger axonal mitochondria; this was true for across different central nervous system tracts as well as across species, including humans. The link between myelin sheath thickness and mitochondrial size was temporarily absent during demyelination but reestablished during advanced remyelination, as shown in two commonly used animal models of toxic demyelination. By further exploring this association in mice with either genetically induced mitochondrial or myelin dysfunction, we show that axonal mitochondrial size adjusts in response to the thickness of the myelin sheath but not *vice versa*. This pinpoints the relevance of mitochondrial adaptation upon myelin repair and might open a new therapeutic window for remyelinating therapies.

KEYWORDS

axons, cuprizone, lysolecithin, mitochondria, myelin, oligodendrocytes, remyelination, transmission electron microscopy

1 | INTRODUCTION

The axon and the surrounding myelin sheath have a very close relationship—morphologically and functionally (Fünfschilling et al., 2012; Stassart et al., 2018). This is, for example, illustrated by the association between axonal diameter and myelin sheath thickness which are both determinants of action potential transduction (Fünfschilling et al., 2012; Hutchinson et al., 1970; Smith et al., 1979). During neuro-inflammatory and/or demyelinating insults, such as multiple sclerosis (MS), this relationship is disrupted. Although the

Edited by Patricia Schuck. Reviewed by Erich Tahara

coherence between the myelin and the axon can be reestablished during subsequent remyelination, the regenerated myelin sheaths are disproportionally thin compared to preinjury condition. Of note, also axons show adaptive mechanisms upon demyelination, for example, increased mitochondria density and/or size compared to homeostatic conditions (Andrews et al., 2006; Mutsaers & Carroll, 1998; Sterky et al., 2011; Zambonin et al., 2011). Mitochondrial size adaptation following injury have also been observed outside the central nervous system (CNS) where mitochondria growth/enlargement is an accepted proxy for cellular adaption to increased energy demand and/or a detrimental response to cellular stress (Jürgensmeier et al., 1998; Pfanner et al., 2019; Suzuki, 1969).

The *g*-ratio is the ratio of the inner-to-outer diameter of a myelinated axons, we serendipitously found a strong correlation between myelin sheath *g*-ratio and axonal mitochondrial size in transmission electron microscopy (TEM) sections from naïve rat corpus callosum (CC). Suggestively, the myelin sheath *g*-ratio and metabolic axonal features do influence each other during homeostatic conditions but also during myelin repair (Chiu, 2011; Chomiak & Hu, 2009; Edgar et al., 2008). We thus explored the association between myelin sheath *g*-ratio and axonal mitochondrial size further in order to consolidate this measurement as a useful tool to assess axon-myelin interdependence and dynamics.

Significance

We herein show that axonal mitochondria, a major axonal energy supplier, closely adjust to corresponding (re)myelination status in different central nervous system tracts and species including humans—but not *vice versa*. These findings emphasize that aiming at restoring axonal energy metabolism during remyelination might be just as important as fostering remyelination during multiple sclerosis, and potentially other demyelinating disorders. This also indicates that the assessment of the correlation between myelin sheath thickness and axonal mitochondrial size might be a superior readout to identify advanced remyelination and reestablishment of homeostatic relation between axon and surrounding myelin compared to traditional readouts.

2 | MATERIALS AND METHODS

2.1 | Species and strains

All mice strains analyzed herein had C75BL/6 genetic background, whereas rats had either Dark agouti or Lewis genetic background. Experimental setup including species, strains, age, sex, cell specificity, phenotype, CNS region, and condition is summarized in Table 1. In brief, spinal cord, CC, or cortical tissue from adult male and female animals were analyzed. The transgenic mice strains analyzed herein include the following: Plp.tg; over-expressing the myelin structure component proteolipid protein 1 (*Plp1*), causing hypomyelination in aged animals. Opa^{Mut}, mtPstI, Afg3L2, and Mfn2 all display mitochondrial dysfunction where Opa^{Mut} comprises 30 coding exons and OPA1 oligomers interfere with mitochondrial quality control mitophagy, and mitochondrial DNA maintenance in the intermembrane space. mtPstI cause double-strand brakes via PstI which is specifically expressed in OL via the PLP promotor. Afg3L2 affects mitochondrial calcium uniporter complex's in the mitochondrial inner membrane. This render effects on mitochondrial protein synthesis and respiration and mitochondrial fragmentation. Mfn2 is the coding gene for Mitofusin2 situated at the outer mitochondrial membrane regulating mitochondrial fusion (Table 1).

2.2 | Models of toxic demyelination

Lysolecithin (lysophosphatidylcholine, LPC) and cuprizone are the most commonly used models of toxic demyelination used in rodents. Experimental details for our material are summarized in Table 2. Lysolecithin injections in the cervical spinal cord were performed as previously described (Blakemore & Franklin, 2008; Carlström et al., 2020; Ineichen et al., 2017): briefly, rats were deeply anesthetized under fentanyl, medetomidine, and midazolam (for Lewis rats) or isoflurane (for Dark agouti rats). Lysolecithin solution (1% in injectable water) was stereotactically injected to either the dorsal funiculus of the cervical spinal cord level C3 (Lewis) or the CC (Dark agouti). For toxic demyelination with cuprizone, mice were maintained with standard rodent chow containing 0.2%–0.3% cuprizone powder (C9012, Sigma-Aldrich, USA) for 5 weeks, followed by normal chow feeding without cuprizone for another week.

2.3 | Selection criteria for TEM images

For TEM imaging, corresponding CNS tissue was postfixed in 1% phosphate-buffered osmium tetroxide (Electron microscopy science) for 4–6 hr, dehydrated in ethanol and propylene oxide (Sigma) and embedded in Epon. Electron microscopic pictures were taken on a Zeiss 10 instrument. Additional TEM images were obtained from original papers and from additional material provided by the authors of herein cited papers, for methodological details refer to Tables 1 and 2. Axonal mitochondria were identified in the transected axons as distinct intra-axonal organelles with clearly defined edges.

Initial assessment of our hypothesis was made in unpublished TEM images from the authors of this study. To further extend our analysis to different species and CNS tracts, authors from key papers were contacted and asked to provide further unpublished TEM images. Finally, particularly for the herein included transgenic mouse strains, we analyzed TEM images from printed publication figures. The following search string was used to identify such publications from Medline: "myelination" AND "transmission electron microscopy" AND "central nervous system". For the transgenic mouse strains, the following string was additionally used: ("PLP" OR "Opa" OR "mtPstI" OR "Afg3L2" OR "Mfn2"). The inclusion criteria for the papers were (a) investigation of myelin ultrastructure using TEM and (b) sufficient resolution of axons, myelin sheaths, and mitochondria,

TABLE 1 Summary strains

Species	Strain	Cell specificity	Phenotype	Age	Sex	CNS region	Condition	Figure	Image Source	Specimen protocol	Ref
Mouse	C57BL/6	N/A	N/A	2 months	M	CC	Naive	1	A	aa	Zou et al. (2020), Steelman et al. (2012)
Rat	DA	N/A	N/A	2 months	M	CC	Naive	1	C	aa	Carlström et al. (2020)
Macaque	N/A	N/A	N/A	N/A	N/A	SC	Naive	1	B	bb, cc	Stikov et al. (2015), Duncan et al. (2018)
Human	N/A	N/A	N/A	N/A	N/A	Prefrontal cortex	Bipolar disorder	1	B	dd	Uranova et al. (2001), Lewis et al. (2019)
Rat	DA	N/A	N/A	2 months	M	CC	10 days post LPC	2	C	aa	Carlström et al. (2020)
Rat	Lewis	N/A	N/A	2–3 months	M	SC (dorsal funiculus)	24 days post LPC	2	C	ee	Ineichen et al. (2017)
Mouse	C57BL/6	N/A	N/A	2–3 months	M	CC	5 weeks of cuprizone	2	A+B	aa	Steelman et al. (2012), Zou et al. (2020)
Mouse	C57BL/6	N/A	N/A	2–3 months	M	CC	1 week post cuprizone withdrawl	2	A+B	aa	Steelman et al. (2012), Zhu et al. (2019)
Mouse	Plp.tg (C57BL/6J)	No	Hypomyelinated axons	Adult	N/A	SC (cervical)	Naïve: $Plp.tg^{-/-}$, $Plp.tg^{+/+}$	3	C	ff	Karim et al. (2007)
Mouse	Opa1Mut (C57BL/6J)	No	Dysfunctional mitochondria	4–9 months	N/A	Optic nerve	Naïve $Opa1Mut^{-/+}$, $Opa1Mut^{+/+}$	3	B	gg, hh	Chao de la Barca et al. (2017), Davies et al. (2007)
Mouse	OL:mtPstI (C57BL/6)	Oligodendrocyte (Plp-Cre)	Mitochondrial DNA break in OL	2–6 months	N/A	SC (thoracic)	Naïve: $OL:mtPstI^{-/-}$, $OL:mtPstI^{+/+}$	3	C	ii	Madsen et al. (2017)
Mouse	Afg3L2 (C57BL/6N)	No	Dysfunctional mitochondria	13–28 weeks	M+F	SC (lumbar)	Naïve: $Afg3L2^{-/-}$, $Afg3L2^{+/+}$	3	B	jj	Wang et al. (2016)
Mouse	Ax:Mfn2 (C57BL/6)	Neurons (Eno2)	Dysfunctional mitochondria in neurons	N/A, N/A	M+F, N/A	SC (lumbar)	Naïve: Ax:MFNR94Q, Ax:MFNWT	3	C	kk	Bernard-Marissal et al. (2019), Cartoni et al. (2010)

Abbreviations: CC, corpus callosum; DA, dark agouti; OL, oligodendrocyte; SC, spinal cord.

Source: A: Analysis of unpublished TEM images. *B*: Analysis of TEM images published in original article including supplementary materials. *C*: Analysis of TEM images published in original article including supplementary materials and additional original images provided by the authors.

TABLE 2 Summary protocol, axonal radius and number of mitochondria

Figure[1]	Species	Genotype/ Condition	Tissue	Protocol[3]	Perf/Fix	Postfix [duration]	*N*	Correlation axonal radius versus mitosize		Mitochondria numbers per axon			Correlation *g*-ratio versus mitosize	
								r^2	*p* value	Median	Min	Max	r^2	*p* value
1C[1]	Mouse	Naive	Corpus callosum	ll	2.5%GA		82	0.2772	<0.0001	1	1	5	0.2259	<0.0001
1C[1]	Mouse	Naive	Corpus callosum	mm	2.%PFA/2.5%GA	2.%PFA/2.5%GA [overnight]	22	0.0645	0.2539	1	1	4	0.2745	0.0123
1D	Rat	Naive	Corpus callosum	aa	1%PFA/2.5%GA	2% OsO4 [2 hr]	61	0.2957	<0.0001	1	1	2	0.3978	<0.0001
1E[1]	Macaque	Naive	Spinal cord	cc	2%Form/2.5%GA		29	0.0341[2]	0.1258[2]	1	1	1	0.4428[2]	<0.0001[2]
1E[1]	Macaque	Naive	Spinal cord	bb	2%PFA/2%GA		43			1	1	1		
1F[1]	Human	Naive	Prefrontal cortex	dd	4%PFA/2.5%GA	4%PFA/2.5%GA [1 week]	7	0.0014[2]	0.8346[2]	1	1	1	0.1304[2]	0.0459[2]
1F[1]	Human	Naive	Prefrontal cortex	dd	4%PFA/2.5%GA	4%PFA/2.5%GA [1 week]	25			1	1	1		
2A	Rat	LPC 10 days	Corpus callosum	aa	1%PFA/2.5%GA	2% OsO4 [2 hr]	39	0.1863	0.3164	2	1	4	0.0176	0.4214
2B	Rat	LPC 24 dpi	Spinal cord	ee	2%Form/2.5%GA	4%Form [4–10 days]	55	0.0326	0.2098	3	1	5	0.1994	0.0012
2C[1]	Mouse	Cuprizone 5 weeks	Corpus callosum	ll	2.5%GA		60	0.0881[2]	0.0314[2]	1	1	7	0.0004[2]	0.8231[2]
2C[1]	Mouse	Cuprizone 5 weeks	Corpus callosum	mm	2.%PFA/2.5%GA	2.%PFA/2.5%GA [overnight]	12			1	1	1		
2D[1]	Mouse	Cuprizone 6 weeks	Corpus callosum	ll	2.5%GA		48	0.1037[2]	0.0040[2]	1	1	3	0.2674[2]	<0.0001[2]
2D[1]	Mouse	Cuprizone 6 weeks	Corpus callosum	mm	2.%PFA/2.5%GA	2.%PFA/2.5%GA [overnight]	29			1	1	1		
3A[1]	Afg3L2	Ctrl	Spinal cord	jj	2%GA	2%GA/1% OsO4	14	0.1003[2]	0.9153[2]	1	1	2	0.2460[2]	0.0033[2]
3A[1]	OPA1	Ctrl	Optic	hh	4%PFA/5%GA	OsO4	10			1	1	1		
3A[1]	OPA1	Ctrl	Optic	gg	2.5%GA		10			1	1	1		
3A	Plp1	Ctrl	Spinal cord	ff	2%PFA/2%GA		26	0.1381	0.1172	1	1	1	0.6698	<0.0001
3A	OL:mtPstI	Ctrl	Spinal cord	ii	4%PFA	2%GA/100mM Suc [o.n.], 2%OsO4 [1 hr]	43	0.0646	0.2539	1	1	3	0.2025	0.0086
3A[1]	MFN2	Ctrl	Spinal cord	kk	2%PFA/2%GA	2%PFA/2%GA [2 hr], OsO4 [4 hr]	13	0.0279[2]	0.3607[2]	2	1	4	0.2535[2]	0.0074[2]
3A[1]	MFN2	Ctrl	Spinal cord	kk	2%PFA/2%GA	2%PFA/2%GA [2 hr], OsO4 [4 hr]	14			2	1	3		
3B[1]	OPA1	KO	Optic	gg	2.5%GA		9	0.0465[2]	0.1136[2]	1	1	1	0.0185[2]	0.2759[2]

(Continues)

TABLE 2 (Continued)

Figure[1]	Species	Genotype/ Condition	Tissue	Protocol[3]	Perf/Fix	Postfix [duration]	*N*	Correlation axonal radius versus mitosize		Mitochondria numbers per axon			Correlation *g*-ratio versus mitosize	
								r^2	*p* value	Median	Min	Max	r^2	*p* value
3B[1]	OPA1	KO	Optic	hh	4%PFA/5%GA	OsO4	15			1	1	1		
3B[1]	Afg3L2	KO	Spinal cord	jj	2%GA	2%GA/1% OsO4	23			1	1	1		
3C[1]	MFN2	KO	Spinal cord	kk	2%PFA/2%GA	2%PFA/2%GA [2 hr], OsO4 [4 hr]	29	0.0207[2]	0.3888[2]	2	1	5	0.0054[2]	0.6450[2]
3C[1]	MFN2	KO	Spinal cord	kk	2%PFA/2%GA	2%PFA/2%GA [2 hr], OsO4 [4 hr]	41			2	1	4		
3C	OL:mtPstI	KO	Spinal cord	ii	4%PFA	2%GA/100 mM Suc [o.n.], 2%OsO4 [1 hr]	40	0.0136	0.4671	1	1	2	0.0056	0.6319
3D	Plp1	KO	Spinal cord	ff	2%PFA/2%GA		46	0.1101	0.9577	1	1	1	0.4990	<0.0001

Notes: [1]TEM images from multiple publications have been pooled to increase "*N*". [2]r^2 and *p* value for the individual dataset included in every figure. When $N < 30$, r^2 and *p* value is given for all the pooled data. [3]*Specimen protocol. [aa]* Perfusion/Fixation: 2.5% glutaraldehyde, 1% paraformaldehyde in 0.1M PBS. Rinsed with 0.1 PBS and postfixed in 2% OsO4 in 0.1M PBS at +4°C for 2 hr Dehydrated in 70%-OH for 30 min +4°C, 95%-OH for 30 min +4°C, 100%-OH 20 min RT, Acetone 2 × 15 min RT, LX-112/Acetone (1:2) 4 hr RT, LX-112/Acetone 1:1 overnight RT, LX-112/Acetone (2:1), overnight RT, LX-112 overnight RT. Embedding: LX-112 at +60°C. *[bb]* Perfusion: 0.9% NaCl and 0.5 ml/L of heparin. Fixation: 2% paraformaldehyde and 2% glutaraldehyde solution. Sectioning: 50 nm. *[cc]* Perfusion/ Fixation: Modified Karnovsky fixative. Embedding: plastic. Sectioning: ultrathin. Imaging: Philips CM120 transmission electron microscope. *[dd]* Perfusion/Fixation: 2.5% glutaraldehyde and 4% paraformaldehyde in 0.1 M PBS for 1 week. Embedding: Rinsed in PBS, 1% osmium tetroxide, stained with uranyl acetate for 1 hr, dehydrated in a series of graded alcohols, and embedded in Araldit epoxy resin. Sectioning: Ultrathin sections. Imaging: Philips EM420. *[ee]* Perfusion: Ringer solution containing 100,000 IU/l Heparin. Fixation: Modified Karnovsky fixative: 2% formalin, 2.5% glutaraldehyde (Axonlab) in 0.1 M phosphate buffer, and 70 mM calcium chloride (Sigma). Postfixed 4–10 days in 4% formalin. Sectioning: 100 nm, with toluidine blue for light microscopy or kept unstained for electron microscopy. Imaging: Zeiss 10. *[ff]* Perfusion: PBS: Fixation: 2% paraformaldehyde and 2% glutaraldehyde solution. Embedding: resin-embedded. Sectioning: Ultrathin. *[gg]* Perfusion: 0.1M PBS. Fixation: 2.5% glutaraldehyde in 0.1M, pH 7.3 in PBS. Sectioning: 85nm, collected and stained with uranyl acetate (1.5% in EtOH 70%). Imaging: Hitachi 7100. *[hh]* Perfusion: PBS. Fixation: 4% paraformaldehyde and 5% glutaraldehyde in cacodylate buffer. Postfixultraed in osmium tetroxide, dehydrated in acetone. Embedding: epoxy resin. Sectioning: Ultrathinsections stained with uranyl acetate and lead citrate. Imaging: Philips CM1000. *[ii]* Animal perfusion: 0.1M PBS Fixation: 4% paraformaldehyde in 0.1M PBS, postfixed overnight in 2% glutaraldehyde plus 100mM sucrose in 0.15M phosphate buffer before incubation with 2% OsO4 for 1 hr. Dehydration in graded ethanol solutions. Embedding: epoxy resin. Sectioning: 60–90 nm. Imaging: Philips CM10. *[jj]* Perfusion: PBS. Fixation: Postfixed in 2% glutaraldehyde in 0.12M PBS, 1% osmium tetroxide, dehydration with ethanol and propylene oxide. Embedding: Epon. Sectioning: 70 nm stained with uranyl acetate and lead citrate. Imaging Phillips CM10. *[kk]* Animal perfusion: 2% paraformaldehyde, 2% glutaraldehyde in 0.1M cacodylate buffer (pH 7.3) for 5min. Fixation: 2% paraformaldehyde, 2% glutaraldehyde, 0.1M cacodylate buffer at pH 7.3 for 2 hr at 4C, and washed in 0.1M cacodylate buffer, and osmicated for 4 hr in 1% OsO4. Embedding: epoxy 812-Araldite. Sectioning: Ultrathin sections collected on cellodin-coated single slot grids and stained with uranyl acetate and lead citrate. Imaging: Technai G2 electron microscope. [II] Perfusion: 0.1 M PBS. Immersed with 2.5% glutaraldehyde TEM fixation solution (Servicebio) and 1% osmic acid in 0.1 M PBS (pH 7.4). Dehydration with ethanol, and embedded with acetone and embedding medium (Servicebio). Sectioning: ultrathin (Leica UC7). Imaging: FEI Tecnai G2 20 TWIN. [mm] Perfusion: 2% paraformaldehyde, 2.5% glutaraldehyde postfix overnight. Washed in 0.1M sodium cacodylate buffer. Stained with 1% osmium tetroxide and 0.5%ptassium ferrocyanide in 0.5% sucrose for 1.5 hr. Dehydraded in alcohol and embedded in epoxy resin. Sectioning: Ultrathin. Imaginge: FEI Morgagni 268 TEM.

that is, individual publication images should have included at least 10 myelinated axons in total. For further details on the exact data source of each analysis, consider Table 1.

2.4 | Statistical analyses

To evaluate myelin thickness correlation with mitochondrial circumference, *g*-ratio (Equation 1) and axonal mitochondria circumference (Equation 2, Figure 1a) were measured using ImageJ with *g*-ratio plugin (Goebbels et al., 2010). Axonal mitochondrial circumference is throughout referred to as axonal mitochondrial size. Axonal mitochondria display a limited variation in circumference, thus truncated axonal mitochondria caught in a TEM cross-section are a representative measurement for the whole organelle (Misgeld et al., 2007). When reanalyzing original and published TEM images, all mitochondria-containing axons were included and analyzed, the mean mitochondrial size was used as the representative measure for every axon. Fixation protocols and its influence on data are in summarized Table 2 and Figure S1b.

$$g\text{–ratio} = \frac{\text{Axonal circumference}}{\text{Myelinated fiber circumference}} \quad (1)$$

$$\bar{y} = \frac{y_1 + \cdots + y_n}{n} \quad (2)$$

All statistical analyses were performed using GraphPad Prism software. All correlation analyses were performed with Pearson's *r* test. Multiple comparisons were throughout analyzed with one-way ANOVA with Bonferroni correction. $p < 0.05$ was considered as statistically significant. No outlier test was applied. Throughout the study, the use of "correlation" and "association" refers to statistically significant relations.

3 | RESULTS

3.1 | During homeostasis, axonal mitochondrial size correlates with myelin g-ratio in rodents, macaques, and humans

Assessment of the axon-myelin ultrastructure and *g*-ratio using TEM is the golden standard for evaluation of homeostatic myelination and remyelination following injury (Franklin & Ffrench-Constant, 2017). The *g*-ratio represents a relative measure for myelin thickness where a *g*-ratio of 1 represents a completely unmyelinated/naked axon and *g*-ratio < 1 represents increasing myelin sheath thickness (Figure 1a, Equation 1). TEM images also offers the opportunity to assess additional ultrastructural features, including axonal mitochondria (Figure 1b, Equation 2).

Since multiple data sets were used in order to obtain sufficient number of axons for every strain and/or conditions, the influence on mitochondrial size from CNS tract, fixation, and postfixation protocols were assessed, and no significant differences were recorded (Figure S1b). Although no significant differences were found in numbers of mitochondria in any of the assessed species or CNS regions (Table 2), *g*-ratio and mitochondrial size varied among the assessed species during homeostatic conditions (Table 1, Figure S1a). Axons with higher *g*-ratio (i.e., thinner myelin sheath) displayed larger axonal mitochondria in rodent CC (Figure 1c,d, Table 1). In addition, mitochondrial size also correlated with axonal radius (Table 2), however this was only evident for rodents. Correlation between axonal mitochondrial size and myelin sheath thickness in relation to axonal diameter was also observed in higher species including macaque spinal cord (Figure 1e, Table 1) (Duncan et al., 2018; Stikov et al., 2015) and human prefrontal cortex (Figure 1f, Table 1) (Lewis et al., 2019; Uranova et al., 2001).

3.2 | Association between myelin g-ratio and axonal mitochondrial size during de- and remyelination

Next, we asked whether myelin-axon units were able to maintain the positive correlation between *g*-ratio and axonal mitochondrial size during de- and remyelination. Two commonly used experimental models to study demyelination and subsequent remyelination are LPC, an intra-parenchymally injected detergent, and cuprizone, a dietary copper-chelating agent (Blakemore & Franklin, 2008; Ineichen et al., 2017; Zendedel et al., 2013).

In the LPC model, the *g*-ratio was unsurprisingly increased during early remyelination (d10 postinjection) compared to advanced remyelination (d24 post injection). In cuprizone-fed mice, a similar decrease in *g*-ratio was observed during demyelination (5 feeding weeks) compared to early remyelination (6 feeding weeks) (Figure S1c). Concomitantly, the axonal mitochondrial size followed the same decrease when comparing the earlier and later time points in both demyelinating models (Figure S1d). Of note, mitochondrial size was similar during advanced remyelination compared to the pre-demyelinating condition.

There was no statistically significant correlation between *g*-ratio and mitochondrial size during the earlier time ,point in neither of the models analyzed (Figure 2a,c). However, during advanced remyelination in LPC and early remyelination in cuprizone, axons with higher *g*-ratio (i.e., thinner myelin sheath) had larger mitochondria, thus re-established the correlation which we observed during homeostasis (Figure 2b,d).

3.3 | Axonal mitochondria adapt their size to dysregulated myelination but not vice versa

Our data indicate a close correlation between *g*-ratio and axonal mitochondrial size during homeostasis and during advanced remyelination. However, the direction of association remains to be identified. In an attempt to address whether axonal mitochondrial size is likely

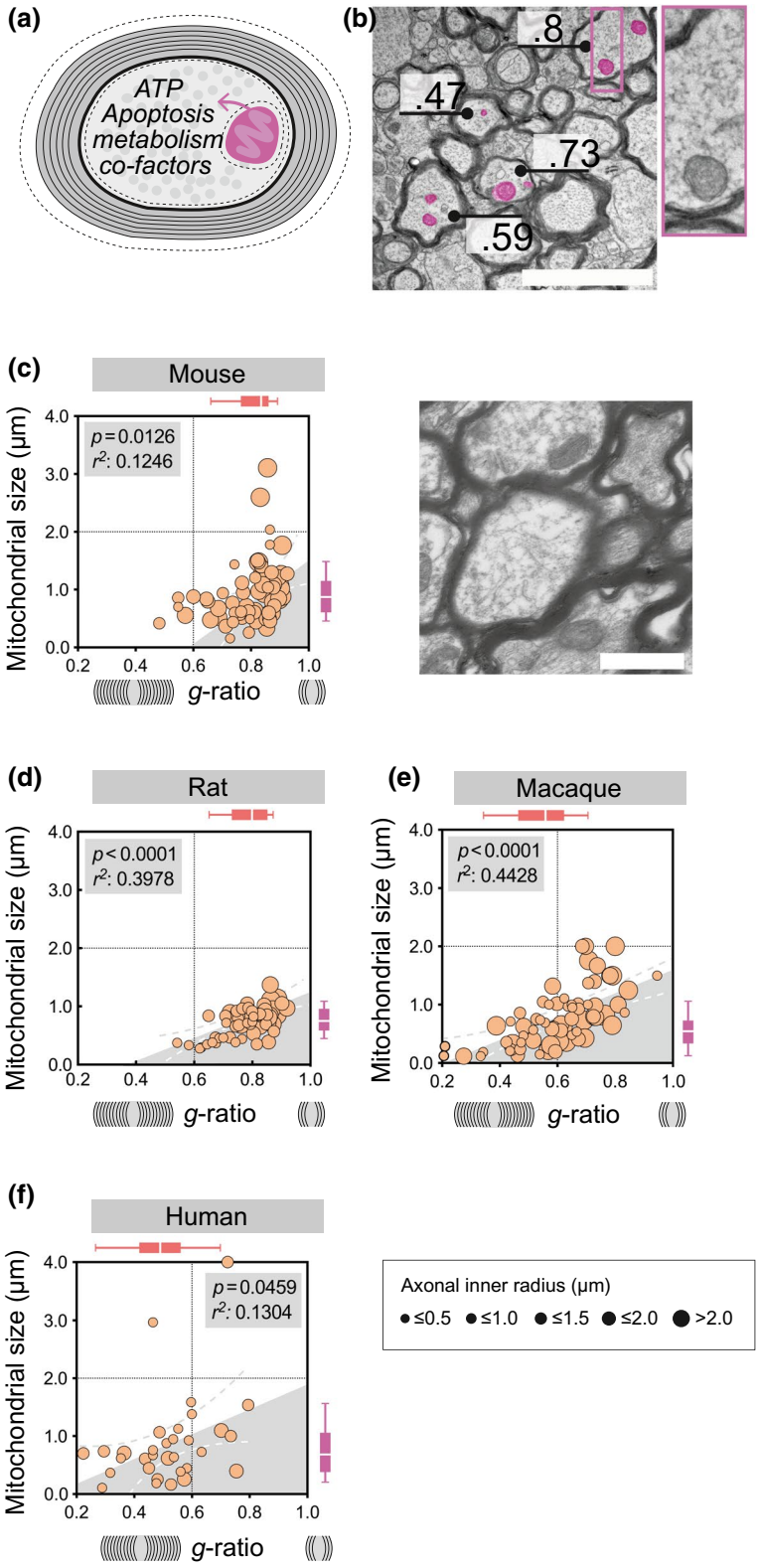

FIGURE 1 Axonal mitochondrial size correlates with myelin *g*-ratio in rodents, macaques, and humans during homeostasis. (a) Illustration of a cross-sectional myelinated axon with the *g*-ratio representing the axonal diameter in relation to the diameter of both the axon and the surrounding myelin. Dashed lines indicate the circumference around the axonal mitochondria, and the inner and outer myelin. (b) Representative transmission electron microscopy (TEM) image with annotated *g*-ratio and, exemplified, pseudo-colored axonal mitochondria in purple (scale-bar 1 µm). (c) Homeostatic mitochondrial size (µm) and *g*-ratio in mouse corpus callosum ($n_{animals} = 3$ $n_{total\ axons} = 104$). Horizontal box plots indicate *g*-ratio, vertical box plots indicate mitochondrial size, whiskers illustrate 10–90 percentile, scale-bar 1 µm. (d) Homeostatic mitochondrial size (µm) and *g*-ratio in rat corpus callosum ($n_{animals} = 3$, $n_{total\ axons} = 61$), representative TEM of rat corpus callosum, scale-bar 2 µm (e) Homeostatic mitochondrial size (µm) and *g*-ratio in macaque spinal cord ($n_{animals} = 3$, $n_{total\ axons} = 72$). (f) Homeostatic mitochondrial size (µm) and *g*-ratio in human prefrontal cortex ($n_{subjects} = 3$, $n_{total\ axons} = 32$). The diameter of each point of measure indicates the axonal inner radius in µm. All correlation analyses were performed with Pearson's *r* test [Color figure can be viewed at wileyonlinelibrary.com]

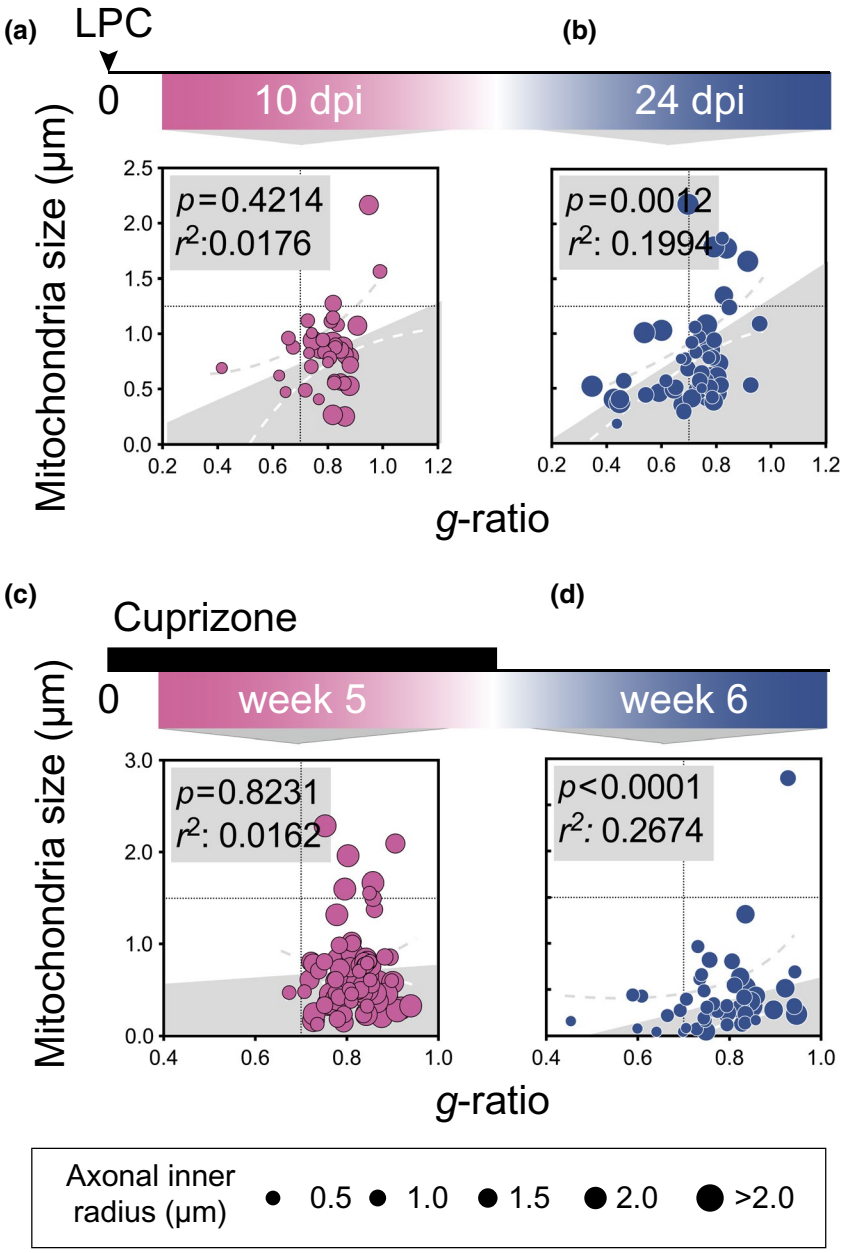

FIGURE 2 Axonal mitochondrial size correlates with myelin sheath *g*-ratio during advanced but not early de- or remyelination. *g*-ratio plotted against axonal mitochondrial size (µm) in rat corpus callosum (CC) (a) 10 days following lysophosphatidylcholine (LPC) injection (early remyelination, $n_{animals} = 3$, $n_{total\ axons} = 39$), and (b) 24 days following LPC injection (advanced remyelination, $n_{animals} = 3$, $n_{total\ axons} = 55$). *g*-ratio plotted against axonal mitochondrial size (µm) in mice CC (c) during cuprizone feeding ($n_{animals} = 3$, $n_{total\ axons} = 72$) and (d) 1 week after cuprizone withdrawal ($n_{animals} = 3$, $n_{total\ axons} = 77$). The diameter of each point of measure indicates the axonal inner radius in µm. All correlation analyses were performed with Pearson's *r* test [Color figure can be viewed at wileyonlinelibrary.com]

to be influenced by myelin sheath *g*-ratio or *vice versa*, TEM images from different mouse strains with either dysfunctional myelination or dysfunctional mitochondria function were assessed (Table 1).

We asked whether dysfunctional mitochondria would be associated with thinner myelin sheaths. For this, we analyzed *g*-ratios and axonal mitochondria in $Opa^{Mut+/+}$ and $Afg3L2^{+/+}$ transgenic mice used as models for dysfunctional mitochondria (Cipolat et al., 2004; Sarzi et al., 2012; Wang et al., 2016) (Table 1). Images were obtained from optic nerve and spinal cord, respectively. Accordingly, both strains displayed increased mitochondrial size compared to corresponding wild-type mice ($Opa^{Mut-/+}$ or $Afg3L2^{-/-}$) (Figure 3a,b, Table 3). However, neither the $Opa^{Mut+/+}$ nor the $Afg3L2^{+/+}$ strain showed changes in *g*-ratio compared to corresponding wild-type mice (Figure 3a,b). Intriguingly, no correlation between *g*-ratio and axonal mitochondrial size was either observed in these strains with mitochondrial dysfunction (Figure 3b,e), that is, mitochondrial size did not seem to affect myelin sheath thickness.

$Opa^{Mut+/+}$ and $Afg3L2^{+/+}$ are full-body mutants, thus mitochondria function is presumably altered in all cells including myelin-generating oligodendrocytes (OLs). Thus, mitochondrial dysfunction in

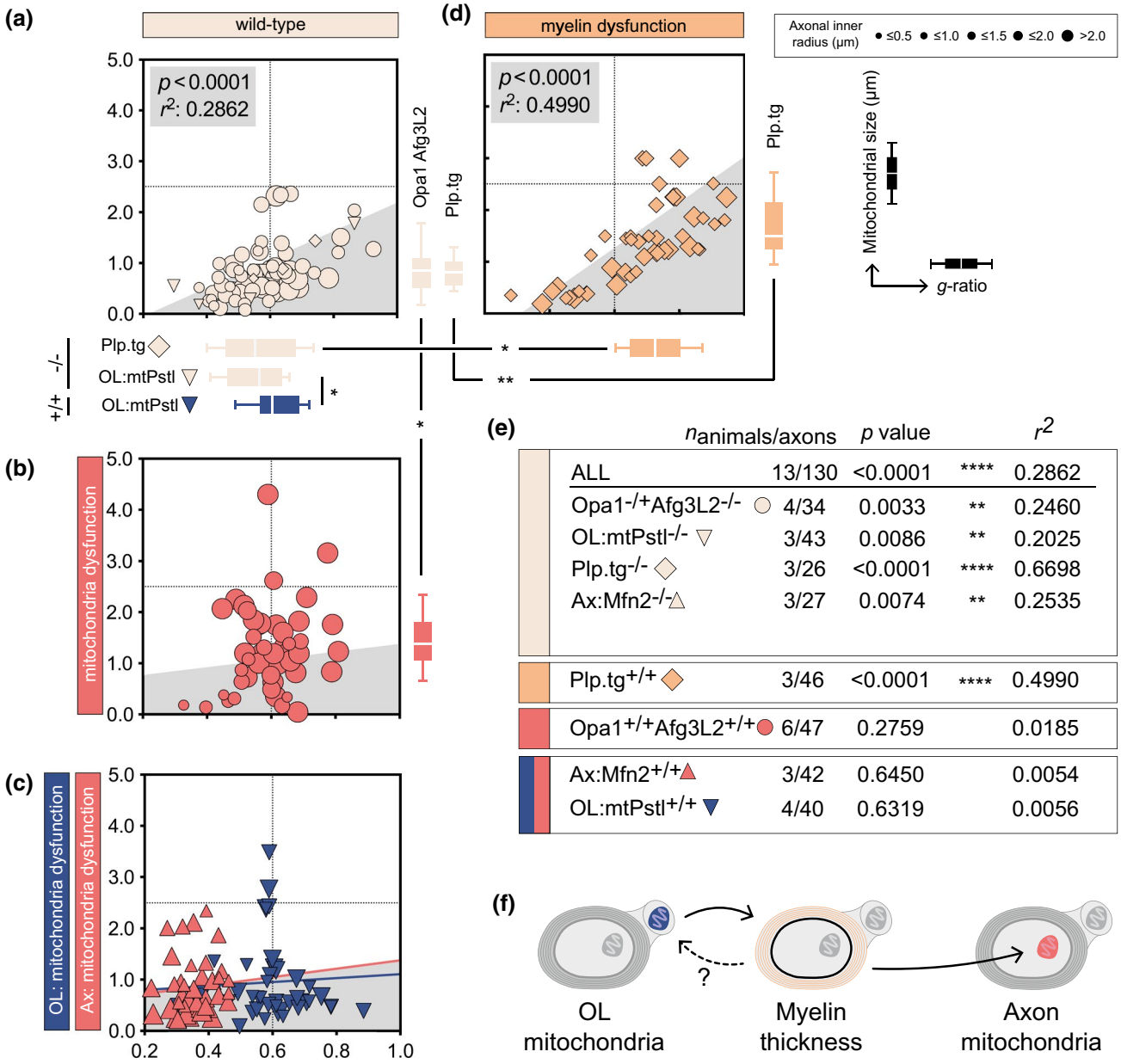

FIGURE 3 Hypomyelination affects axonal mitochondrial size but not *vice versa*. (a) Homeostatic mitochondrial size (µm) and *g*-ratio in mice with genetically induced mitochondrial dysfunction. Horizontal box plots indicate *g*-ratio, vertical box plots indicate mitochondrial size, whiskers illustrate 10–90 percentile. (b) Homeostatic mitochondrial size (µm) and *g*-ratio genetically induced mitochondrial dysfunction ($n_{animals} = 6$, $n_{axons} = 47$). (c) Homeostatic mitochondrial size (µm) and *g*-ratio in Ax:Mfn2$^{+/+}$ ($n_{animals} = 3$, $n_{axons} = 40$) and OL:mtPstI$^{+/+}$ ($n_{animals} = 4$, $n_{axons} = 40$) mice. (d) Homeostatic mitochondrial size (µm) and *g*-ratio in Plp.tg$^{+/+}$ mice ($n_{animals} = 3$, $n_{axons} = 46$). (e) Statistical summary of correlation between *g*-ratio and axonal mitochondrial size in all mice strains. (f) Schematic illustration of the adaption hierarchy where OL mitochondrial dysfunction influences *g*-ratio (i.e., myelin thickness) which in turn influence axonal mitochondrial size. All correlation analyses were performed with Pearson's *r* test, multiple comparisons of mitochondrial size and *g*-ratio in (a–d) were performed using one-way ANOVA. $^{*}p < 0.05$, $^{**}p < 0.01$ [Color figure can be viewed at wileyonlinelibrary.com]

OLs could be responsible for the lack of *g*-ratio adaption to axonal mitochondrial dysfunction. To address this, lumbar spinal cord of mice with axonal-specific mutations in the mitochondria protein Mfn2 (here referred to as Ax:Mfn2) were assessed (Bernard-Marissal et al., 2019). However, similar to the full-body mutant strains (Opa$^{Mut+/+}$ and Afg3L2$^{+/+}$) the myelin sheaths did not adapt in the Ax:Mfn2$^{+/+}$ in response to dysfunctional axonal mitochondria, thus leaving the *g*-ratio unchanged compared to wild type (Ax:Mfn2$^{-/-}$) (Figure 3a,c,e). To verify whether OL-specific loss of mitochondria function could influence *g*-ratio, sections from lumbar spinal cord of mice expressing mtPstI under the Plp promoter (here referred to as OL:mtPstI), causing mitochondria DNA-breakage, were analyzed (Wang et al., 2016). OL:mtPstI transgenic mice showed a higher *g*-ratio (i.e., a thinner myelin sheath) compared to corresponding control

TABLE 3 Summary statistics

	Mitochondrial size		G-ratio		
	Mean ± *SD*	*p* value[a]	Mean ± *SD*	*P* value[a]	*N*
Opa1Mut$^{-/+}$ Afg3L2$^{-/-}$	0.71 ± 0.47	*	0.55 ± 0.11	0.3162	34
Opa1Mut+/+ Afg3L2$^{+/+}$	1.26 ± 0.84		0.59 ± 0.10		47
OL:mtPstI$^{-/-}$	0.74 ± 0.54	0.2410	0.55 ± 0.08	*	43
OL:mtPstI$^{+/+}$	0.91 ± 0.76		0.61 ± 0.09		40
Plp.tg$^{-/-}$	0.78 ± 0.47	**	0.61 ± 0.12	*	26
Plp.tg$^{+/+}$	1.36 ± 0.78		0.68 ± 0.15		46
Ax:Mtf2$^{-/-}$	0.69 ± 0.27	0.1743	0.36 ± 0.07	0.3603	27
Ax:Mtf2$^{+/+}$	0.85 ± 0.56		0.34 ± 0.07		42

[a]Means compared with one-way ANOVA.

*$p < 0.05$, **$p < 0.01$.

mice (Figure 3a,c). OL:mtPstI$^{+/+}$ animals did also exhibit increased axonal mitochondrial size however not significant ($p = 0.2410$) (Table 3). In line with the observations in Opa1, Afg3L2, and Ax:Mfn2 strains, *g*-ratio and axonal mitochondrial size did not correlate (Figure 3e).

We next asked whether thinner myelin sheaths be associated with increased mitochondrial size. The Plp.tg$^{+/+}$ mice display hypomyelination due to knock-in of *Plp1* (Karim et al., 2007) (Table 1). Hypomyelination was confirmed by an increased *g*-ratio in Plp.tg$^{+/+}$ mice compared to wild-type mice (Plp.tg$^{-/-}$) (Figure 3a,d, Table 3). In Plp.tg$^{+/+}$ mice, axons with increased *g*-ratio (i.e., thinner myelin sheath) displayed increased axonal mitochondrial size (Figure 3a,d,e).

4 | DISCUSSION

The axon and its surrounding myelin have a close relationship. Yet, fundamental understanding of their mutual regulation processes, particularly with regard to axonal energy metabolism, is lacking. We herein explored the interplay between *g*-ratio (as proxy for myelin sheath thickness in relation to axonal diameter) and axonal mitochondrial size by reanalyzing original and published data sets. This means multiple data sets were included for the study, however neither tract or perfusion/fixation protocol nor post-fixation protocol did statistically significantly affect axonal mitochondrial size.

During homeostasis, *g*-ratio and size of axonal mitochondria were consistently correlated among different species and CNS tracts, that is, that axons with increased *g*-ratio displayed larger mitochondria. This association was lost during demyelination and reestablished during advanced remyelination in two animal models of toxic demyelination. Finally, assessment of mutant mice strains with either dysfunctional myelin or mitochondria revealed that mitochondrial size adapts to dysfunctional myelination.

The axonal energy metabolism is highly complex: axons are dependent of at least two different energy sources—direct local supply of ATP by axonal mitochondria as well as lactate supply via monocarboxylate transporters in the OLs (Fünfschilling et al., 2012; Lee et al., 2012; Saab et al., 2013). Moreover, both distribution and morphology of axonal mitochondria has been reported to change over time and between different conditions, for example, during aging (Edgar et al., 2008; Stahon et al., 2016). Furthermore, the *in situ* evidence of mitochondrial proteins such as Complex IV are also altered simultaneously to morphological and/or distributional changes (Barron et al., 2004; Kirkinezos et al., 2005; Mahad et al., 2008, 2009).

During demyelinating insults, for example, after stroke, Alzheimer's disease, or, likely most thoroughly studied in this regard, MS, the axonal energy metabolism shifts out of balance. Different axonal metabolic responses aim at compensating this insufficient axonal energy metabolism—with the coalition of these processes termed "axonal mitochondrial response to demyelination" (Campbell & Mahad, 2012; Campbell et al., 2014; Kiryu-Seo et al., 2010). These processes include increase in mitochondrial number, activity and speed of mitochondrial transport.

Our findings are in line with this concept and further extend it, it has been speculated that the ability to mount this response may be confined to a subset of neurons (Campbell & Mahad, 2012; Mahad et al., 2009). Our data indicate that this response may in fact be employable by different strategic CNS tracts including the CC and the corticospinal tract in the spinal cord. Furthermore, our data indicate that also in homeostatic conditions, mitochondria dynamically adjust to myelin sheath thickness (as potential proxy for lactate supply of axons) in higher mammals including humans.

Noteworthy, remyelination only partially reverses the axonal energy deficiency that follows demyelination (Campbell & Mahad, 2012). It might thus be warranted to use more sophisticated measures to evaluate (re) myelination than solely measuring *g*-ratio, for example, myelin sheath thickness and size of axonal mitochondria as conducted in our analysis.

Using the Plp.tg model, our data further suggest that axonal mitochondrial size adjust to changes in myelin sheath *g*-ratio. This was however not true when OL:mtPstI$^{+/+}$ exhibited higher *g*-ratio as the

Plp.tg strain but without significant changes in axonal mitochondrial size. Possibly the use of a genetic model indirectly generating a high *g*-ratio via mtPstI may influence axonal mitochondrial size in a way which is absent in Plp.tg model.

This might hint toward the OLs compensatory capacity axonal energy during imbalance is limited. Thus, aiming at restoring axonal energy metabolism during remyelination might be just as important as fostering remyelination during MS, and potentially other demyelinating disorders.

The restrictions of our study are the potential selection bias caused by partially analyzing printed publication figures and the inclusion of multiple data sets in order to increase the number of measured data points. However, main findings were confirmed in additional original material. For data transparency we have also displayed relevant raw data for every individual data set. Data sets of dysfunctional mitochondria characterized with TEM are rare and thus affecting the number of measurable data points. Since we (to our knowledge) have analyzed all available data sets fulfilling the above criteria, we are confident that our samples are reflecting the true biology. Moreover, the findings were robust when investigating different species, mutant strains, and CNS regions. Additionally, cuprizone has been described to increase mitochondrial size via direct mitochondrial toxicity (Suzuki, 1969). In this study, we cannot specify whether these in relations to each other are dependent or independent events. However, also in LPC, the correlation between *g*-ratio and axonal mitochondria thickness is reestablished during advanced remyelination, thereby corroborating this correlation as consistent feature of advanced remyelination.

Our findings underline the dynamic response of mitochondria to a changing myelin landscape during homeostasis, de- and remyelination. Such regulative processes could be exploited as potential therapeutic target, for example, for demyelinating disorders where axons are at high risk for demise due to insufficient axonal energy supply. Furthermore, assessment of the correlation between *g*-ratio and axonal mitochondrial size might be a superior readout to identify advanced remyelination and reestablishment of homeostatic relation between axon and surrounding myelin.

DECLARATION OF TRANSPARENCY

The authors, reviewers and editors affirm that in accordance to the policies set by the *Journal of Neuroscience Research*, this manuscript presents an accurate and transparent account of the study being reported and that all critical details describing the methods and results are present.

ACKNOWLEDGMENTS

We acknowledge Prof. Fredrik Piehl for mentoring. We acknowledge Dr. Roberta Brambilla, Dr. Mark McLaughlin, University of Glasgow; Dr. Nathalie Bernard-Marissal, École Polytechnique Fédérale de Lausanne; Dr, Roman Chrast, Karolinska Institute; and Dr. Jun Wang, Fudan University for kindly providing TEM images.

CONFLICT OF INTEREST

The authors declare no conflict of interest.

AUTHOR CONTRIBUTION

Conceptualization, K.E.C. *Investigation*, K.E.C., B.V.I. and K.Z. *Writing - original draft*, K.E.C. *Writing - review & editing*, K.E.C., B.V.I. and K.Z.

PEER REVIEW

The peer review history for this article is available at https://publons.com/publon/10.1002/jnr.24767.

DATA AVAILABILITY STATEMENT

All data owned by authors are available upon request.

ORCID

Keying Zhu https://orcid.org/0000-0001-7500-1532
Karl E. Carlström https://orcid.org/0000-0002-3001-2403

REFERENCES

Andrews, H., White, K., Thomson, C., Edgar, J., Bates, D., Griffiths, I., Turnbull, D., & Nichols, P. (2006). Increased axonal mitochondrial activity as an adaptation to myelin deficiency in the Shiverer mouse. *Journal of Neuroscience Research*, *83*, 1533–1539.

Barron, M. J., Griffiths, P., Turnbull, D. M., Bates, D., & Nichols, P. (2004). The distributions of mitochondria and sodium channels reflect the specific energy requirements and conduction properties of the human optic nerve head. *British Journal of Ophthalmology*, *88*, 286–290.

Bernard-Marissal, N., van Hameren, G., Juneja, M., Pellegrino, C., Louhivuori, L., Bartesaghi, L., Rochat, C., El Mansour, O., Médard, J. J., Croisier, M., & Maclachlan, C. (2019). Altered interplay between endoplasmic reticulum and mitochondria in Charcot-Marie-Tooth type 2A neuropathy. *Proceedings of the National Academy of Sciences of the United States of America*, *116*, 2328–2337.

Blakemore, W. F., & Franklin, R. J. M. (2008). Remyelination in experimental models of toxin-induced demyelination. *Current Topics in Microbiology and Immunology*, *318*, 193–212.

Campbell, G. R., & Mahad, D. J. (2012). Mitochondrial changes associated with demyelination: Consequences for axonal integrity. *Mitochondrion*, *12*, 173–179. https://doi.org/10.1016/j.mito.2011.03.007

Campbell, G. R., Worrall, J. T., & Mahad, D. J. (2014). The central role of mitochondria in axonal degeneration in multiple sclerosis. *Multiple Sclerosis Journal*, *20*, 1806–1813.

Carlström, K. E., Zhu, K., Ewing, E., Krabbendam, I. E., Harris, R. A., Falcão, A. M., Jagodic, M., Branco, G. C., & Piehl, F. (2020). Gsta4 controls apoptosis of differentiating adult oligodendrocytes during homeostasis and remyelination via the mitochondria-associated Fas-Casp8-Bid-axis. *Nature Communications*, *11*, 4071–4113.

Cartoni, R., Arnaud, E., Médard, J.-J., Poirot, O., Courvoisier, D. S., Chrast, R., Martinou, J.-C. (2010). Expression of mitofusin 2R94Q in a transgenic mouse leads to Charcot–Marie–Tooth neuropathy type 2A. *Brain*, *133*(5), 1460–1469. https://doi.org/10.1093/brain/awq082

Chao de la Barca, J. M., Simard, G., Sarzi, E., Chaumette, T., Rousseau, G., Chupin, S., Gadras, C., Tessier, L., Ferré, M., Chevrollier, A., Desquiret-Dumas, V., Gueguen, N., Leruez, S., Verny, C., Miléa, D., Bonneau, D., Amati-Bonneau, P., Procaccio, V., Hamel, C., … Prunier-Mirebeau, D. (2017). Targeted metabolomics reveals early dominant optic atrophy signature in optic nerves of Opa1delTTAG/+ mice. *Investigative Opthalmology & Visual Science*, *58*(2), 812. https://doi.org/10.1167/iovs.16-21116

Chiu, S. Y. (2011). Matching mitochondria to metabolic needs at nodes of Ranvier. *Neuroscientist*, *17*, 343–350.

Chomiak, T., & Hu, B. (2009). What is the optimal value of the g-ratio for myelinated fibers in the rat CNS? A theoretical approach. *PLoS ONE*, *4*, e7754.

Cipolat, S., Martins de Brito, O., Dal Zilio, B., & Scorrano, L. (2004). OPA1 requires mitofusin 1 to promote mitochondrial fusion. *Proceedings of the National Academy of Sciences of the United States of America*, *101*, 15927–15932.

Davies, V. J., Hollins, A. J., Piechota, M. J., Yip, W., Davies, J. R., White, K. E., Nicols, P. P., Boulton, M. E., & Votruba, M. (2007). Opa1 deficiency in a mouse model of autosomal dominant optic atrophy impairs mitochondrial morphology, optic nerve structure and visual function. *Human Molecular Genetics*, *16*(11), 1307–1318. https://doi.org/10.1093/hmg/ddm079

Duncan, I. D., Radcliff, A. B., Heidari, M., Kidd, G., August, B. K., & Wierenga, L. A. (2018). The adult oligodendrocyte can participate in remyelination. *Proceedings of the National Academy of Sciences of the United States of America*, *115*, E11807–E11816.

Edgar, J. M., McCulloch, M. C., Thomson, C. E., & Griffiths, I. R. (2008). Distribution of mitochondria along small-diameter myelinated central nervous system axons. *Journal of Neuroscience Research*, *86*, 2250–2257.

Franklin, R. J. M., & Ffrench-Constant, C. (2017). Regenerating CNS myelin—From mechanisms to experimental medicines. *Nature Reviews Neuroscience*, *18*, 753–769.

Fünfschilling, U., Supplie, L. M., Mahad, D., Boretius, S., Saab, A. S., Edgar, J., Brinkmann, B. G., Kassmann, C. M., Tzvetanova, I. D., Möbius, W., & Diaz, F. (2012). Glycolytic oligodendrocytes maintain myelin and long-term axonal integrity. *Nature*, *485*, 517–521.

Goebbels, S., Oltrogge, J. H., Kemper, R., Heilmann, I., Bormuth, I., Wolfer, S., Wichert, S. P., Möbius, W., Liu, X., Lappe-Siefke, C., & Rossner, M. J. (2010). Elevated phosphatidylinositol 3,4,5-trisphosphate in glia triggers cell-autonomous membrane wrapping and myelination. *Journal of Neuroscience*, *30*, 8953–8964.

Hutchinson, N. A., Koles, Z. J., & Smith, R. S. (1970). Conduction velocity in myelinated nerve fibres of *Xenopus laevis*. *Journal of Physiology*, *208*, 279–289.

Ineichen, B. V., Kapitza, S., Bleul, C., Good, N., Plattner, P. S., Seyedsadr, M. S., Kaiser, J., Schneider, M. P., Zörner, B., Martin, R., & Linnebank, M. (2017). Nogo-A antibodies enhance axonal repair and remyelination in neuro-inflammatory and demyelinating pathology. *Acta Neuropathologica*, *134*, 423–440.

Jürgensmeier, J. M., Xie, Z., Deveraux, Q., Ellerby, L., Bredesen, D., & Reed, J. C. (1998). Bax directly induces release of cytochrome c from isolated mitochondria. *Proceedings of the National Academy of Sciences of the United States of America*, *95*, 4997–5002.

Karim, S. A., Barrie, J. A., McCulloch, M. C., Montague, P., Edgar, J. M., Kirkham, D., Anderson, T. J., Nave, K. A., Griffiths, I. R., & Mclaughlin, M. (2007). PLP overexpression perturbs myelin protein composition and myelination in a mouse model of Pelizaeus-Merzbacher disease. *Glia*, *55*, 341–351.

Kirkinezos, I. G., Bacman, S. R., Hernandez, D., Oca-Cossio, J., Arias, L. J., Perez-Pinzon, M. A., Bradley, W. G., & Moraes, C. T. (2005). Cytochrome c association with the inner mitochondrial membrane is impaired in the CNS of G93A-SOD1 mice. *Journal of Neuroscience*, *25*, 164–172.

Kiryu-Seo, S., Ohno, N., Kidd, G. J., Komuro, H., & Trapp, B. D. (2010). Demyelination increases axonal stationary mitochondrial size and the speed of axonal mitochondrial transport. *Journal of Neuroscience*, *30*, 6658–6666.

Lee, Y., Morrison, B. M., Li, Y., Lengacher, S., Farah, M. H., Hoffman, P. N., Liu, Y., Tsingalia, A., Jin, L., Zhang, P. W., & Pellerin, L. (2012). Oligodendroglia metabolically support axons and contribute to neurodegeneration. *Nature*, *487*, 443–448.

Lewis, A. J., Genoud, C., Pont, M., van de Berg, W. D., Frank, S., Stahlberg, H., Shahmoradian, S. H., & Al-Amoudi, A. (2019). Imaging of post-mortem human brain tissue using electron and X-ray microscopy. *Current Opinion in Structural Biology*, *58*, 138–148.

Madsen, P. M., Pinto, M., Patel, S., McCarthy, S., Gao, H., Taherian, M., Karmally, S., Pereira, C. V., Dvoriantchikova, G., Ivanov, D., Tanaka, K. F., Moraes, C. T., & Brambilla, R. (2017). Mitochondrial DNA double-strand breaks in oligodendrocytes cause demyelination, axonal injury, and CNS inflammation. *The Journal of Neuroscience*, *37*(42), 10185–10199. https://doi.org/10.1523/jneurosci.1378-17.2017

Mahad, D. J., Ziabreva, I., Campbell, G., Lax, N., White, K., Hanson, P. S., Lassmann, H., & Turnbull, D. M. (2009). Mitochondrial changes within axons in multiple sclerosis. *Brain*, *132*, 1161–1174. https://doi.org/10.1093/brain/awp046

Mahad, D., Ziabreva, I., Lassmann, H., & Turnbull, D. (2008). Mitochondrial defects in acute multiple sclerosis lesions. *Brain*, *131*, 1722–1735. https://doi.org/10.1093/brain/awn105

Misgeld, T., Kerschensteiner, M., Bareyre, F. M., Burgess, R. W., & Lichtman, J. W. (2007). Imaging axonal transport of mitochondria in vivo. *Nature Methods*, *4*, 559–561.

Mutsaers, S. E., & Carroll, W. M. (1998). Focal accumulation of intra-axonal mitochondria in demyelination of the cat optic nerve. *Acta Neuropathologica*, *96*, 139–143. https://doi.org/10.1007/s00410050873

Pfanner, N., Warscheid, B., & Wiedemann, N. (2019). Mitochondrial proteins: From biogenesis to functional networks. *Nature Reviews Molecular Cell Biology*, *20*, 267–284.

Saab, A. S., Tzvetanova, I. D., & Nave, K.-A. (2013). The role of myelin and oligodendrocytes in axonal energy metabolism. *Current Opinion in Neurobiology*, *23*, 1065–1072.

Sarzi, E., Angebault, C., Seveno, M., Gueguen, N., Chaix, B., Bielicki, G., Boddaert, N., Mausset-Bonnefont, A. L., Cazevieille, C., Rigau, V., & Renou, J. P. (2012). The human OPA1delTTAG mutation induces premature age-related systemic neurodegeneration in mouse. *Brain*, *135*, 3599–3613.

Smith, K. J., Blakemore, W. F., & McDonald, W. I. (1979). Central remyelination restores secure conduction. *Nature*, *280*, 395–396. https://doi.org/10.1038/280395a0

Stahon, K. E., Bastian, C., Griffith, S., Kidd, G. J., Brunet, S., & Baltan, S. (2016). Age-related changes in axonal and mitochondrial ultrastructure and function in white matter. *Journal of Neuroscience*, *36*, 9990–10001.

Stassart, R. M., Möbius, W., Nave, K.-A., & Edgar, J. M. (2018). The axon-myelin unit in development and degenerative disease. *Frontiers in Neuroscience*, *12*, 467.

Steelman, A. J., Thompson, J. P., & Li, J. (2012). Demyelination and remyelination in anatomically distinct regions of the corpus callosum following cuprizone intoxication. *Neuroscience Research*, *72*(1), 32–42. https://doi.org/10.1016/j.neures.2011.10.002

Sterky, F. H., Lee, S., Wibom, R., Olson, L., & Larsson, N.-G. (2011). Impaired mitochondrial transport and Parkin-independent degeneration of respiratory chain-deficient dopamine neurons in vivo. *Proceedings of the National Academy of Sciences of the United States of America*, *108*, 12937–12942. https://doi.org/10.1073/pnas.1103295108

Stikov, N., Campbell, J. S. W., Stroh, T., Lavelée, M., Frey, S., Novek, J., Nuara, S., Ho, M. K., Bedell, B. J., Dougherty, R. F., & Leppert, I. R. (2015). Quantitative analysis of the myelin g-ratio from electron microscopy images of the macaque corpus callosum. *Data Brief*, *4*, 368–373.

Suzuki, K. (1969). Giant hepatic mitochondria: Production in mice fed with cuprizone. *Science*, *163*, 81–82.

Uranova, N., Orlovskaya, D., Vikhreva, O., Zimina, I., Kolomeets, N., Vostrikov, V., & Rachmanova, V. (2001). Electron microscopy of oligodendroglia in severe mental illness. *Brain Research Bulletin*, *55*, 597–610.

Wang, S., Jacquemyn, J., Murru, S., Martinelli, P., Barth, E., Langer, T., Niessen, C. M., & Rugarli, E. I. (2016). The mitochondrial m-AAA protease prevents demyelination and hair greying. *PLoS Genetics*, *12*, e1006463.

Zambonin, J. L., Zhao, C., Ohno, N., Campbell, G. R., Engeham, S., Ziabreva, I., Schwarz, N., Lee, S. E., Frischer, J. M., Turnbull, D. M., Trapp, B. D., Lassmann, H., Franklin, R. J. M., & Mahad, D. J. (2011). Increased mitochondrial content in remyelinated axons: Implications for multiple sclerosis. *Brain*, *134*, 1901–1913. https://doi.org/10.1093/brain/awr110

Zendedel, A., Beyer, C., & Kipp, M. (2013). Cuprizone-induced demyelination as a tool to study remyelination and axonal protection. *Journal of Molecular Neuroscience*, *51*, 567–572.

Zhu, K., Sun, J., Zou, Z., Wu, X., Wang, Y., Wu, G., Harris, R. A., Wang, J. (2019). Repurposing of omeprazole for oligodendrocyte differentiation and remyelination. *Brain Research*, *1710*, 33–42. https://doi.org/10.1016/j.brainres.2018.12.037

Zou, Z., Sun, J., Kang, Z., Wang, Y., Zhao, H., Zhu, K., & Wang, J. (2020). Tyrosine kinase receptors Axl and MerTK mediate the beneficial effect of electroacupuncture in a cuprizone-induced demyelinating model. *Evidence-Based Complementary and Alternative Medicine*, *2020*, 1–13. https://doi.org/10.1155/2020/3205176

SUPPORTING INFORMATION

Additional supporting information may be found online in the Supporting Information section.

FIGURE S1 (a) Summary of *p* values following multiple comparisons assessing homeostatic *g*-ratio (red gradient) and mitochondrial size (μm) (purple gradient) between different species (mouse (Ms), rat (Rt), macaque (Mc), and human (Hu). (b) Mitochondrial size (μm) of all herein acquired mitochondria grouped by tissue (left). Mitochondrial size grouped by perfusion/fixation protocols (middle) and postfixation protocols (right). (c) *g*-ratio and (d) axonal mitochondrial size (μm) in LPC and cuprizone model of toxic demyelination. All analyses were performed using one-way ANOVA, multiple comparisons between all means (a, b) and to naïve condition in (c, d). $^{*}p < 0.05$, $^{**}p < 0.01$, $^{***}p < 0.001$

Transparent Peer Review Report

Transparent Science Questionnaire for Authors

How to cite this article: Ineichen BV, Zhu K, Carlström KE. Axonal mitochondria adjust in size depending on *g*-ratio of surrounding myelin during homeostasis and advanced remyelination. *J Neurosci Res*. 2021;99:793–805. https://doi.org/10.1002/jnr.24767